Article:
Guo, H., Li, Y., Zhao, B. et al. (4 more authors) (2025) Transient dynamic characteristics of floating bush structure of marine high pressure fuel pump. Physics of Fluids, 37 (8). 083603. ISSN: 1070-6631

https://doi.org/10.1063/5.0278455

Transient Dynamic Characteristics of Floating Bush Structure of Marine High Pressure Fuel Pump

Huaiqian Guo [a], Yazhou Li[b, c], Bin Zhao [a, *], Yuan Guo[d], Zhongliang Xie [e], Ardian MORINA [a, f], Xiqun Lu [a]

[a] College of Power and Energy Engineering, Harbin Engineering University, Harbin 150001, China;

[b.] School of Design, Shanghai Jiao Tong University, Shanghai 20030, China;

[c] Business Development Department, Chongqing Hongjiang Machinery Co. Ltd., Chongqing 402160, China;

[d] Technology Center, Chongqing Hongjiang Machinery Co. Ltd., Chongqing 402160, China;

[e] Department of Engineering Mechanics, Northwestern Polytechnical University, Xi'an 710072, China;

[f] School of Mechanical Engineering, University of Leeds, Leeds LS2 9JT, UK

Abstract:

The roller-floating bush-pin (RFBP) structure is an important component in high-pressure fuel pumps of marine diesel engines, and its dynamic characteristics have a significant impact on equipment stability. In this study, a simulation model of the transient dynamic characteristics of the double-layer oil film structure was established, taking into account the thermoelastic effect of the structure and the time-varying operating conditions in the fuel pump. A double-layer oil film lubrication system test platform was developed to validate the precision of the simulation model. A comparative analysis was performed to evaluate dynamic parameters of both inner and outer oil films, and the influence of operational parameters and structural parameters on the dynamic characteristics of the structure was studied. It shows that the double-layer oil film structure can significantly reduce the stiffness and damping of the structure compared to the single-layer oil film structure. The dynamic characteristics of the inner oil film exhibit greater sensitivity to variations in operating and structural parameters. The outer oil film has a more pronounced effect on the equivalent dynamic characteristics of the RFBP structure than the inner oil film.

Keywords: Marine diesel engine; Cam-roller; RFBP structure; Dynamic characteristics.

---

* Corresponding author. E-mail address: donglizhaobin@hrbeu.edu.cn (B. Zhao)

1. Introduction:

The high-pressure fuel pump is a crucial component of the engine system, and is essential for ensuring efficient fuel combustion. The cam mechanism in the high-pressure fuel pump which includes the RFBP structure is shown in Fig.1. During the operation of the fuel pump, the fuel pressure acts on the roller through the plunger. The cam drives the roller to rotate, and the roller drives the floating bush to rotate while the roller pin is a fixed component. The RFBP structure has double layer oil films: one layer is the oil film between the roller pin and the floating bush, and the other layer is formed between the floating bush and the roller. The floating bush has a certain rotational speed, and it can reduce the relative speed between the roller and the roller pin, thereby reducing temperature rise and thermal deformation of the RFBP structure [1-5]. The lubrication performance of the RFBP structure is a critical factor affecting mechanical stability. Meanwhile, the dynamic characteristics of the RFBP structure, which are based on the lubrication properties, serve as critical boundary conditions for the vibration analysis of the fuel pump shaft system and also play an essential role in the stability of marine diesel engine equipment. Consequently, constructing a transient dynamics model for the RFBP structure becomes essential to evaluate how operational and structural parameters influence its dynamic performance.

Recently, many studies have explored bearings designed with two-layer oil films, among which turbocharger floating ring bearings (FRBs) stand out as the most common example. The lubrication characteristics are regarded as the standard for evaluating the lubrication status and also as the foundation of studies of the dynamic characteristics. Many scholars had conducted studies on the lubrication characteristics of the FRB structure. Some of them have analyzed the lubrication properties of FRBs with varying structures [6-12]. For instance, Soni et al. [6-7] studied the lubrication characteristics of non-circular FRBs and found that this structure can increase the bearing capacity compared to standard FRBs. Pei et al. [8] demonstrated that surface texturing can effectively reduce thermal elevation in floating ring bearing lubricants. Yang et al. [9] found that FRBs with dislocated structures can increase operational stability. Wang et al. [10] demonstrated that the turbocharger oscillation levels can be effectively mitigated through adjustments in manufacturing clearance configurations. Kang et al. [11] found that floating ring oil holes can reduce end leakage temperature rise. The related studies look into the effect of varying structures of the lubrication

characteristics, and the lubrication model is a little simplified, mostly using the fluid dynamic pressure lubrication model. Dong et al. [12] conducted studies on the lubrication performance of on three-lobe semi-floating ring bearing and discovered that as the oil supply pressure and temperature increase, the temperature rise and maximum oil film pressure gradually decrease. Some scholars had improved the lubrication simulation models of FRBs and considered more influencing factors [13-19]. Andres et al. [13-15] considered the influences of oil thermal effects and floating ring heat transfer in the lubrication model of FRBs. Peng et al. [16] studied the lubrication state of FRBs under poor working conditions, considering the cavitation effect under poor oil lubrication. Qin et al. [17] established a steady-state lubrication model of the FRBs based on Reynolds equation and random rough model. Novotný et al. [18] established an effective computational model of the rotor FRB system so as to work out the transient problems of turbocharger rotor dynamics. Yang et al. [19] used analytical methods to calculate the elastic deformation of the floating ring and considering it in the lubrication model, it was found that the inner surface exhibited obviously higher deformation surface compared to the outer surface.

In addition, as the dynamic characteristics of FRBs play an important role in the stability of rotor-FRBs system of turbochargers, researchers have also conducted a series of studies in this area [20-25]. Zhao et al. [20] developed a fluid lubrication model for FRBs, performing a preliminary analysis into the stiffness and damping characteristics of inner/outer oil films through minor perturbation analysis. Guang et al. [21] developed a turbocharger rotor model using finite element methods, incorporating stiffness and damping characteristics from floating ring bearings. The study found that the large cross stiffness of the bearings is the main reason of the self-excited whirl motion. Guo et al. [22,23] developed a lubrication model for the FRB structure with deep and shallow cavities, and computed the stiffness/damping coefficients of the FRB structure. Based on this, they explored the influence of rotor stiffness and floating ring mass on the stability of the floating ring bearing rotor system. Wang et al. [24] analyzed the effect of current intensity on the stiffness coefficient of FRBs with magnetic pole structures. Xie et al. [25] developed a lubrication calculation model for FRBs taking rough surfaces into account. On this basis, the effect of operating and structural parameters on the stiffness and damping coefficients of the bearings was systematically studied. The above research mainly focuses on the FRB structure with double-layer oil films, and its structural characteristic is

the same as the RFBP structure. Since FRBs usually operate in stable state, the studies on stiffness/damping coefficients are mainly conducted in the steady state. Zhang et al. [26] studied the nonlinear vibration problem of a floating ring bearing rotor system based on the dynamic characteristics of the floating ring bearings' oil film, finding that variations in bearing eccentricity at higher rotational speeds lead to complex rotor dynamics due to the cross-coupled stiffness and damping of the inner and outer oil films. However, unlike the FRB structure, the RFBP structure usually operates under transient conditions, so it is essential to establish a dynamic characteristic analysis model under transient conditions. In addition, the operating mode of the FRB structure is significantly different from that of the RFBP structure. During the operation of the FRB structure, the internal rotor drives the floating ring to rotate, and the roller of the RFBP structure is driven by the cam, which in turn drives the floating bush to rotate. As a result, the cam-roller dynamics and kinematic behavior should be considered in the lubrication and dynamic characteristics analysis model of RFBP structure, and the characteristic is not present in FRBs.

Currently, research on the lubrication and dynamic characteristics of the RFBP structure remains limited, whereas studies of the roller-pin structure, which serves the same function in fuel pumps are more extensive. Z. El-Goul et al. [27] studied the wear morphology characteristics of the roller and pin surface from three different materials after frictional experiments. Shivam S et al. [28-30] analyzed the lubrication properties of the roller-pin structure and found that elastic deformation in roller/pin components positively impacts contact-point film thickness distribution. The current research on the RFBP structure is mostly focused on steady-state conditions, and the lubrication characteristics of the structure is mainly studied. However, the research on the dynamic characteristics of the RFBP structure is still not sufficient. Yuan [31] established a hydrodynamic lubrication model for the RFBP structure under stable operating conditions in high-pressure fuel pumps and studied its load-bearing capacity. Li [32] established a fluid steady-state lubrication model with a double-layer oil film structure in a fuel pump based on the Fluent software, taking into account the influence of the cavitation effect. Xiao et al. [33] studied the lubrication state of RFBP structure under stable operating conditions and found that the lubrication state of the inner oil film has a guiding role in the design of the friction pair structure of the structure. Guo et al. [34] conducted studies on the transient

lubrication characteristics of the RFBP structure, and the time-varying lubrication characteristic were obtained.

In summary, studies on the lubrication properties of the RFBP structure in marine diesel engine fuel pumps remain limited, and research into its transient dynamic characteristics grounded in these properties is even scarcer. Moreover, the studies on double-layer oil film lubrication structures mainly focus on the FRB structure in turbochargers, while the RFBP structure in this work is greatly different from the FRB structure. The FRB structure usually works in stable conditions, while the RFBP structure in this work is under transient conditions, and the operating mode is also significantly different from the FRB structure. Given the critical role of the RFBP structure's dynamic characteristics in fuel pump vibration analysis, establishing a dynamic characteristic model under transient operating conditions is essential. For this reason, the cam-roller dynamic and kinematic model was coupled with the transient lubrication model of the RFBP structure, considering the thermoelastic effect of the structure. The method of small disturbance was used to calculate the dynamic characteristics of the RFBP structure. The study compared dynamic characteristics of the inner and outer oil films, while assessing the impact of working conditions and structural factors on system performance. The results provide valuable guidance for RFBP design optimization.

Nomenclature

c_p	Lubrication oil specific heat(J/(kg·K))	W_i, W_o	Friction losses of inner/outer films(W)
d_z	Plunger diameter(m)	$\ddot{x}_1$, $\ddot{y}_1$	x/y acceleration of floating bush(m/s^2)
e_c	Cam eccentricity(m)	$\ddot{x}_2$, $\ddot{y}_2$	Acceleration of roller(m/s^2)
F	Load on roller(N)	α	Cam angle(°)
F_0	Spring preload force(N)	Δx, Δy	x/y directions displacement disturbances(μm)
h_i, h_o	The thickness of inner/outer films(μm)	Δu, Δv	Velocity disturbances in x/y directions
k_s	Stiffness of plunger spring(N·m)	δ_{Pi}, δ_{Po}	Elastic deformation of inner/outer layers(μm)
KI, ***KO***	Inner/outer layers elastic deformation matrices	δ_{Ti}, δ_{To}	Inner/outer layers Thermal deformation (μm)
L	Width of floating bush(m)	ε_i, ε_o	Eccentricity of inner/outer layers
m_1, m_2	Floating bush/roller mass(kg)	θ	Angle of oil film(°)
P_{ix}, P_{iy}	x/y reaction force of inner film(N)	θ', θ''	Angle of oil film before/after disturbance(°)
P_{ox}, P_{oy}	x/y reaction force of outer film(N)	μ_i, μ_o	Inner/outer lubrication oil viscosity (Pa·s)
p_x, p_y	Ratios of oil film pressure to Δx and Δy	ρ	Density of lubrication oil(kg/m^3)
p_u, p_v	Ratios of oil film pressure to Δu and Δv	σ_i, σ_o	Inner/outer comprehensive roughness(m)
Q_i, Q_o	Inner/outer films end leakage flow rate(ml/s)	Γ_i, Γ_o	Friction torque of inner/outer layers (N·m)
R_i, R_o	Inner/outer radius of floating bush(m)	φ	Cam pressure angle (°)
s_α	Cam lift(m)	φ_i, φ_o	Deviation angles of inner/outer layers (°)
t	Operating time(s)	ϕ_c, ϕ_s	Contact /Shear flow factor
T_i, T_o	Inner/outer oil films temperature(℃)	ϕ_x, ϕ_y	Pressure flow factor
T_s	Inlet oil temperature(℃)	ω_2, ω_f	Roller/floating bush speed(rad/s)

2. Theoretical model

2.1 Cam-roller model

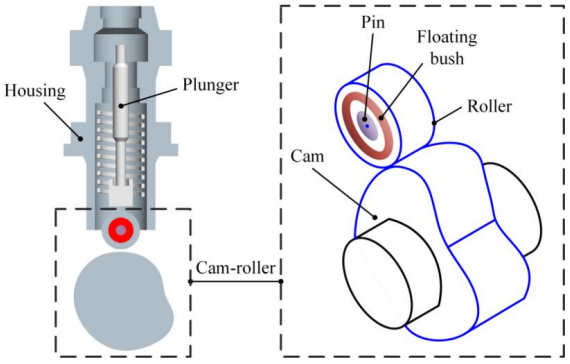

Fig.1. Cam mechanism structure in fuel pump.

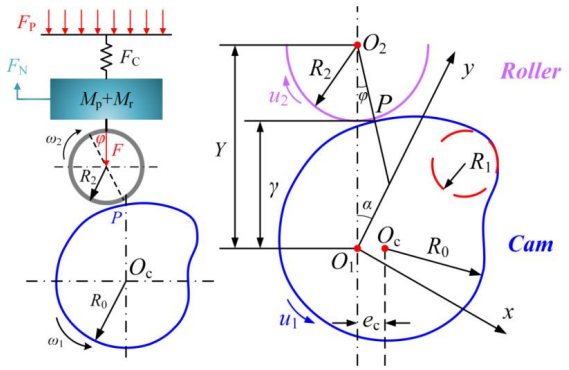

Fig.2. Schematic diagram of cam-roller model in fuel pump.

Fig.2 shows the model of the cam-roller utilized in the fuel pump mechanism of the diesel engine. The cam drives the roller to rotate, and the roller drives the floating bush to rotate while the roller pin is a fixed component. It can be seen that the force F on the roller mainly consists of three parts, including the fuel force of the plunger F_P, the inertial force of roller followers F_N, and the plunger spring force F_C [35]. M_p is the mass of plunger and other related component, and M_r is the mass of roller and followers. φ is the pressure angle of the cam mechanism. O_1 is the center of rotation of the cam, and O_c is the center of base circle. R_0 is the base circle radius, and R_1 is the cam curvature radius. R_2 is the outer radius of the roller. The rotational speed of the cam and roller are denoted as ω_1 and ω_2, respectively. u_1 and u_2 are the surface velocity of cam and roller, respectively. Y and γ are the vertical heights of the roller center and contact point P, respectively.

2.1.1 Cam-roller dynamic model

The dynamic load equation of the roller under the time-varying conditions is as follow:

$$F\cos\varphi = \underbrace{F_0 + k_s \cdot s_\alpha}_{F_C} + \underbrace{M\omega_1^2 \frac{d^2 s_\alpha}{d\alpha^2}}_{F_N} + \underbrace{0.25\pi d_2^2 \cdot \left[p_1 + (p_1 - p_2) \cdot s_\alpha / s_{\max}\right]}_{F_P} \quad (1)$$

Because the fuel pressure curve is related to the cam lift in the mechanical high-pressure fuel pump, the extreme value of the fuel pressure and the cam lift curve is given to interpolate F_P, and the Newton interpolation method is used, where $(p_1\text{-}p_2)/s_{\max}$ is the difference quotient in Newton interpolation. The peak/lowest values of the fuel pressure are p_1 and p_2, respectively. M is the mass

driven by cam, which is the sum of M_p and M_r. The pressure angle φ is mathematically defined by the following equation:

$$\varphi = \arctan\frac{|s_\alpha - e_c|}{s_\alpha + \sqrt{R_0^2 - e_c^2}}. \tag{2}$$

2.1.2 Cam-roller kinematic model

It can be seen from Fig. 2, there are geometric relationships in the cam mechanisms, as follow:

$$\begin{cases} Y = \gamma + R_2 \\ \gamma = s_\alpha + R_0 \end{cases}. \tag{3}$$

For the curvature radius of the fuel pump cam R_1, the calculation formula is:

$$R_1 = \frac{\left[Y^2 + \left(\frac{\mathrm{d}Y}{\mathrm{d}\alpha}\right)^2\right]^{\frac{3}{2}}}{Y^2 + 2\left(\frac{\mathrm{d}Y}{\mathrm{d}\alpha}\right)^2 - Y\frac{\mathrm{d}^2Y}{\mathrm{d}\alpha^2}} - R_2 \cdot \tag{4}$$

The derivative of the roller height (Y) in the y-direction with the cam angle is the roller velocity in the y-direction, while the second derivative of the roller height (Y) in the y-direction with the cam angle is the roller acceleration in y-direction. The velocity of cam (u_1) and roller (u_2) can be calculated as follow:

$$u_1 = \omega_1 \cdot R_{1-2},\ u_2 = \omega_2 \cdot R_2, \tag{5}$$

where $R_{1\text{-}2}$ is the comprehensive curvature radius of the cam-roller, and the calculation formula of $R_{1\text{-}2}$ is:

$$\frac{1}{R_{1-2}} = \frac{1}{R_1} + \frac{1}{R_2}. \tag{6}$$

The roller velocity u_2 can be solved by the following equation [36]:

$$u_2 = u_1 + \omega_1 R_2 \frac{\left(\frac{\mathrm{d}\gamma}{\mathrm{d}\alpha}\right)^2 - \gamma\frac{\mathrm{d}^2\gamma}{\mathrm{d}\alpha^2}}{\gamma^2 + \left(\frac{\mathrm{d}\gamma}{\mathrm{d}\alpha}\right)^2}. \tag{7}$$

The roller speed (ω_2) can be obtained by combining formula (6) and (7).

2.2 Lubrication analysis model

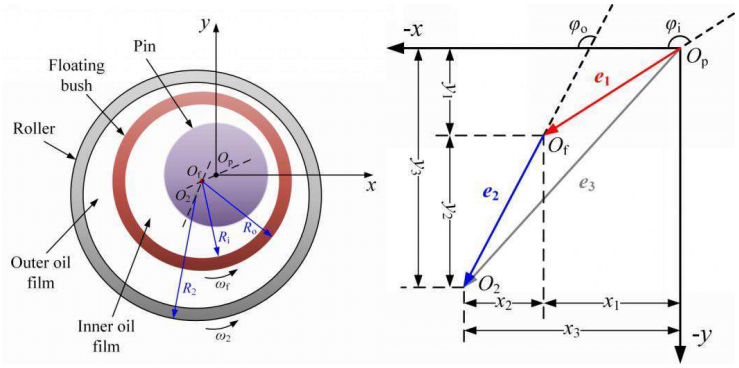

(a) (b)

Fig.3. Diagram of the transient model of RFBP structure.
(a) Middle plane of the RFBP structure (b) Relative position.

Fig.3 presents the transient model of the RFBP structure. Fig.3(a) presents the middle plane of the RFBP structure. At first, the center of the floating bush and the roller were both located at point O_p, which is the center of the roller pin. Under the action of external loads, the floating bush center moves to Point O_f, while the roller center moves to Point O_2. Fig.3(b) presents the coordinate system of dynamic model. e_1 and e_3 represent the eccentricities of the floating bush center and roller center, respectively, both relative to the pin center. e_2 represents the eccentricity of the roller center relative to the floating bush center.

The fluid pressure of inner/outer layers (p_i, p_o) of the floating bush is expressed by the Eqs.(8) and (9) [37]:

$$\frac{\partial}{R_i^2\partial\theta}\left(\phi_x\frac{\rho h_i^3}{\mu_i}\frac{\partial p_i}{\partial\theta}\right)+\frac{\partial}{\partial y}\left(\phi_y\frac{\rho h_i^3}{\mu_i}\frac{\partial p_i}{\partial y}\right)=6\omega_f\phi_c\frac{\partial(\rho h_i)}{\partial\theta}-6\omega_f\sigma_i\frac{\partial(\rho\phi_s)}{\partial\theta}+12\phi_c\frac{\partial h_i}{\partial t}, \tag{8}$$

$$\begin{aligned}&\frac{\partial}{R_o^2\partial\theta}\left(\phi_x\frac{\rho h_o^3}{\mu_o}\frac{\partial p_o}{\partial\theta}\right)+\frac{\partial}{\partial y}\left(\phi_y\frac{\rho h_o^3}{\mu_o}\frac{\partial p_o}{\partial y}\right)=6(\omega_f+\omega_2)\phi_c\frac{\partial(\rho h_o)}{\partial\theta}\\&+6(\omega_f-\omega_2)\sigma_o\frac{\partial(\rho\phi_s)}{\partial\theta}+12\phi_c\frac{\partial h_o}{\partial t}\end{aligned}, \tag{9}$$

where, h_i and h_o represent the thickness of the inner/outer oil film, respectively. p_i and p_o represent the pressure of the inner/outer oil film. ϕ_x, and ϕ_y are the parameters of pressure and flow rate, are used to express the effect of surface roughness on lubricating fluid in the two-dimensional horizontal direction. ϕ_s is the shear flow rate parameter of lubricating fluid, used to express the additional flow rate caused by the roughness of the upper and lower surfaces of the friction pair when they move

relative to each other. ϕ_s is the shear flow rate parameter of lubricating fluid, used to characterize the interference of rough peak contact on lubrication behavior under mixed lubrication conditions. The pressure distribution of the inner/outer films is described under transient shear and squeeze flow.

The Reynolds boundary conditions are used to express oil film pressure, as follows:

$$p\big|_r = p_a,\ \left.\frac{\partial p}{\partial \theta}\right|_r = 0 \tag{10}$$

p is the oil film pressure, θ is the circumferential angle of the oil film, and p_a is the inlet oil pressure. The subscript (r) represents the position of oil film rupture.

The film thickness of inner/outer layers (h_i, h_o) of the floating bush is expressed by the Eqs.(11) and (12):

$$h_i = \left(c_i + \delta_{Ti}\right)\left(1 + \varepsilon_i \cos\left(\theta - \varphi_i\right)\right) + \delta_{Pi}, \tag{11}$$

$$h_o = \left(c_o + \delta_{To}\right)\left(1 + \varepsilon_o \cos\left(\theta - \varphi_o\right)\right) + \delta_{Po}, \tag{12}$$

where δ_{Ti} and δ_{Ti} represent the clearance change caused by thermal deformation of the inner and outer layers respectively, calculated by Eqs.(13) and (14):

$$\delta_{Ti} = \left(\alpha_f - \alpha_p\right) R_i \Delta T_i, \tag{13}$$

$$\delta_{To} = \left(\alpha_r - \alpha_f\right) R_o \Delta T_o, \tag{14}$$

where α_P, α_f and α_r are the thermal expansion coefficients of the roller pin, floating bush and roller, respectively. ΔT_i and ΔT_o represent the temperature rise of the inner and outer films respectively.

Under the slow-speed and heavy-load working conditions, the elastic deformation cannot be ignored in calculation. This work includes the elastic deformation of the floating bush [34]. Since the pressure of the inner film has higher than the outer film, elastic deformation increases the thickness of the inner film and decreases the thickness of the outer film. Elastic deformation of the floating bush (δ_{Pi}, δ_{Po}) can be obtained through Eqs.(15) and (16):

$$\delta_{Pi}\left(\theta, y\right) = \int_0^L \int_0^{2\pi} KI\left(\theta, y\right) p_i\left(\theta, y\right) d\theta dy, \tag{15}$$

$$\delta_{Po}\left(\theta, y\right) = \int_0^L \int_0^{2\pi} KO\left(\theta, y\right) p_o\left(\theta, y\right) d\theta dy, \tag{16}$$

where $\delta_{pi}(\theta,y)$ and $\delta_{po}(\theta,y)$ are the elastic deformations of the inner and outer layers of the floating bushing at the node (θ, y) respectively. $p_i(\theta, y)$, $p_o(\theta, y)$ are the oil film pressure at node (θ, y) for the inner and outer layers of the floating bushing respectively.

T is used to uniformly described the oil films temperature (T_i: inner, T_o: outer), which can be expressed as:

$$T = T_s + k\frac{W}{c_p \rho Q}, \tag{17}$$

where, ΔT represents temperature variations in both oil film layers (ΔT_i: inner, ΔT_o: outer), W denotes friction power for each layer (W_i/W_o), and Q corresponds to end leakage flow rates (Q_i/Q_o) at respective films. Since it's necessary to account for conduction heat dissipation under low-speed and heavy load conditions, and the heat will not be completely carried away by the terminal leakage, the temperature rise coefficient k is taken as 0.8 [38].

Eq.(18) provides the equations for determining the radial and axial displacement trajectories of the floating bush.

$$\begin{cases} m_1 \ddot{x}_1 = P_{xi} - P_{xo} \\ m_1 \ddot{y}_1 = P_{yi} - P_{yo} + m_1 g \end{cases}. \tag{18}$$

Eq.(19) provides the equations for determining the radial and axial displacement trajectories of the roller.

$$\begin{cases} m_2 \ddot{x}_2 = P_{xo} \\ m_2 \ddot{y}_2 = F - P_{yo} \end{cases}. \tag{19}$$

Eq.(20) provides the equations for determining the transient velocity of the floating bush.

$$I_1 \dot{\omega}_f = \Gamma_i - \Gamma_o, \tag{20}$$

where Γ_i and Γ_o represent to the friction torque of the inside and outside layers of the floating bush respectively.

2.3 Dynamic characteristic model of RFBP structure

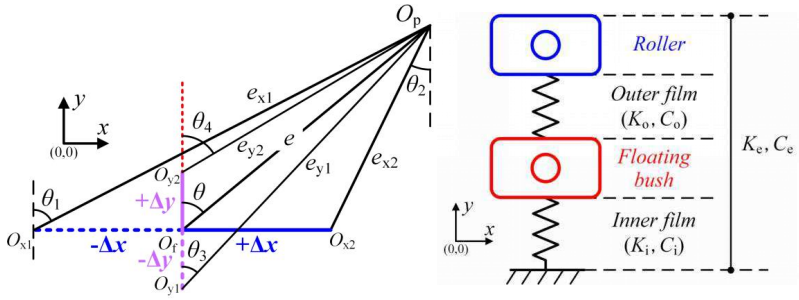

(a) (b)

Fig.4. Dynamic characteristic model of the RFBP structure.
(a) Schematic diagram of micro disturbance method (b) Equivalent dynamic characteristics.

Fig.4 is a schematic diagram of the dynamic characteristic model, and the principle of the micro disturbance method is shown in Fig.4(a). Here, the inner oil film is taken as an example. When disturbed by -Δx and +Δx in the x-direction, the floating bush center (O_f) moves to positions O_{x1} and O_{x2} respectively. The center of the floating bush (O_f) reaches O_{x1} and O_{x2} after a disturbance displacement of -Δx and +Δx in the x-direction. The eccentricities after disturbance are e_{x1} and e_{x2}. θ_1 and θ_2 are the starting and ending angles of the oil film, which refer to the direction angles after disturbance is generated. After disturbance displacement of -Δy and +Δy in the y-direction, the center of the floating bush reaches O_{y1} and O_{y2}. The eccentricities after disturbance are e_{y1} and e_{y2}. θ_3 and θ_4 represent the initial and final angles of the oil film. θ' and θ'' are used to uniformly represent the oil film position angle before and after disturbance as follows, and the stiffness coefficient of the inner oil film is calculated by equation (21):

$$\begin{bmatrix} K_{xx} & K_{yx} \\ K_{xy} & K_{yy} \end{bmatrix}_i = \int_0^L \int_{\theta'}^{\theta''} -\begin{bmatrix} p_x \\ p_y \end{bmatrix}_i \left[\cos\theta \ \ \sin\theta\right] dxdy \tag{21}$$

where p_x and p_y are the ratios of the oil film pressure after the disturbance to x and y at a certain moment under transient conditions. L is the length of the floating bush. The stiffness coefficient of the outer oil film is calculated by equation (21):

$$\begin{bmatrix} K_{xx} & K_{yx} \\ K_{xy} & K_{yy} \end{bmatrix}_o = \int_0^L \int_{\theta'}^{\theta''} -\begin{bmatrix} p_x \\ p_y \end{bmatrix}_o \left[\cos\theta \ \ \sin\theta\right] dxdy \tag{22}$$

The damping coefficients of oil films are determined using the velocity perturbation method, with inner and outer film values derived from equations (23) and (24) respectively.

$$\begin{bmatrix} C_{xx} & C_{yx} \\ C_{xy} & C_{yy} \end{bmatrix}_i = \int_0^L \int_{\theta'}^{\theta''} -\begin{bmatrix} p_u \\ p_v \end{bmatrix}_i \left[\cos\theta \ \ \sin\theta\right] dxdy \tag{23}$$

$$\begin{bmatrix} C_{xx} & C_{yx} \\ C_{xy} & C_{yy} \end{bmatrix}_o = \int_0^L \int_{\theta'}^{\theta''} -\begin{bmatrix} p_u \\ p_v \end{bmatrix}_o \left[\cos\theta \ \ \sin\theta\right] dxdy \tag{24}$$

where p_u and p_v represent the dimensionless ratios of oil film pressure to velocity perturbations in x/y-axis directions at a certain moment under transient conditions. In addition, the main stiffness coefficients are expressed as K_{xx} and K_{yy}, while K_{xy} and K_{yx} are the cross stiffness coefficients. The main damping coefficients are expressed as C_{xx} and C_{yy}, while C_{xy} and C_{yx} are the cross damping coefficients.

As illustrated in Fig.3(b), the RFBP structure is a dual fluid-film bearings in series arrangement. The inner/outer film stiffness (K_i/K_o) and damping (C_i/C_o) parameters are distinctly labeled. In

addition, the equivalent stiffness/damping coefficients of the RFBP structure are expressed by K_e and C_e, respectively. The system's main and cross-coupled stiffness/damping values are calculated as follows:

$$\begin{Bmatrix} \frac{1}{K_{xx}} & \frac{1}{K_{xy}} \\ \frac{1}{K_{yx}} & \frac{1}{K_{yy}} \end{Bmatrix}_e = \begin{Bmatrix} \frac{1}{K_{xx}} & \frac{1}{K_{xy}} \\ \frac{1}{K_{yx}} & \frac{1}{K_{yy}} \end{Bmatrix}_i + \begin{Bmatrix} \frac{1}{K_{xx}} & \frac{1}{K_{xy}} \\ \frac{1}{K_{yx}} & \frac{1}{K_{yy}} \end{Bmatrix}_o \tag{25}$$

$$\begin{Bmatrix} \frac{1}{C_{xx}} & \frac{1}{C_{xy}} \\ \frac{1}{C_{yx}} & \frac{1}{C_{yy}} \end{Bmatrix}_e = \begin{Bmatrix} \frac{1}{C_{xx}} & \frac{1}{C_{xy}} \\ \frac{1}{C_{yx}} & \frac{1}{C_{yy}} \end{Bmatrix}_i + \begin{Bmatrix} \frac{1}{C_{xx}} & \frac{1}{C_{xy}} \\ \frac{1}{C_{yx}} & \frac{1}{C_{yy}} \end{Bmatrix}_o \tag{26}$$

Since the dynamic characteristics of RFBP are associated with external factors, including structural dimensions and rotational speed, as well as internal factors such as eccentricity and misalignment angle, the dimensionless stiffness/damping coefficients are used to eliminate the impact of external factors on dynamic characteristics and facilitate a more intuitive analysis of the results [39]. The relative units of dimensionless stiffness coefficients of the inner/outer films are taken as $\mu_i\omega_f L/\psi_i^2$, $\mu_o(\omega_2-\omega_f)L/\psi_o^2$. The relative units of dimensionless damping coefficients of the inner/outer films are taken as $\mu_i L/\psi_i^2$, $\mu_o L/\psi_o^2$. ψ_i and ψ_o are the inner and outer relative clearance, respectively. The inner relative clearance is the ratio of the inner clearance to the inner radius of the floating bush, and the outer relative clearance is the ratio of the outer clearance to the outer radius of the floating bush. The inner film dimensionless stiffness coefficients are expressed as $\overline{K}_{i,xx}$, $\overline{K}_{i,xy}$, $\overline{K}_{i,yx}$, $\overline{K}_{i,yy}$, and $\overline{K}_{o,xx}$, $\overline{K}_{o,xy}$, $\overline{K}_{o,yx}$, $\overline{K}_{o,yy}$ are the outer film dimensionless stiffness coefficients. The inner film dimensionless damping coefficients are expressed as $\overline{C}_{i,xx}$, $\overline{C}_{i,xy}$, $\overline{C}_{i,yx}$, $\overline{C}_{i,yy}$, and $\overline{C}_{o,xx}$, $\overline{C}_{o,xy}$, $\overline{C}_{o,yx}$, $\overline{C}_{o,yy}$ are the outer film dimensionless damping coefficients. In addition, the equivalent stiffness coefficients of the RFBP structure are $\overline{K}_{e,xx}$, $\overline{K}_{e,xy}$, $\overline{K}_{e,yx}$, $\overline{K}_{e,yy}$, and the equivalent damping is $\overline{C}_{e,xx}$, $\overline{C}_{e,xy}$, $\overline{C}_{e,yx}$, $\overline{C}_{e,yy}$.

2.4 The solution procedure

Fig.5 shows the numerical analysis flow chart of transient dynamic characteristics calculation of the RFBP structure. The cam-roller model is calculated to obtain transient operating conditions of the RFBP structure, and the results are taken as the input for the RFBP structure dynamic characteristics calculation model. The elasticity of the structure and the thermal effect of the lubrication oil were considered in the model. The calculation was completed when the motion trajectory of the roller and floating bush closed, respectively, within the cycle. The super relaxation iteration is implemented to

accelerate the calculation speed, the super relaxation iteration coefficient is selected between 1.0 and 2.0, and in the current work the Iterative coefficient is taken as 1.7. The convergence accuracy of pressure calculation is 10^{-6}. The displacement disturbances of the inner/outer oil films are both 1.0μm. The velocity disturbances of the inner/outer oil films are set to 0.01 times the relative rotational speed.

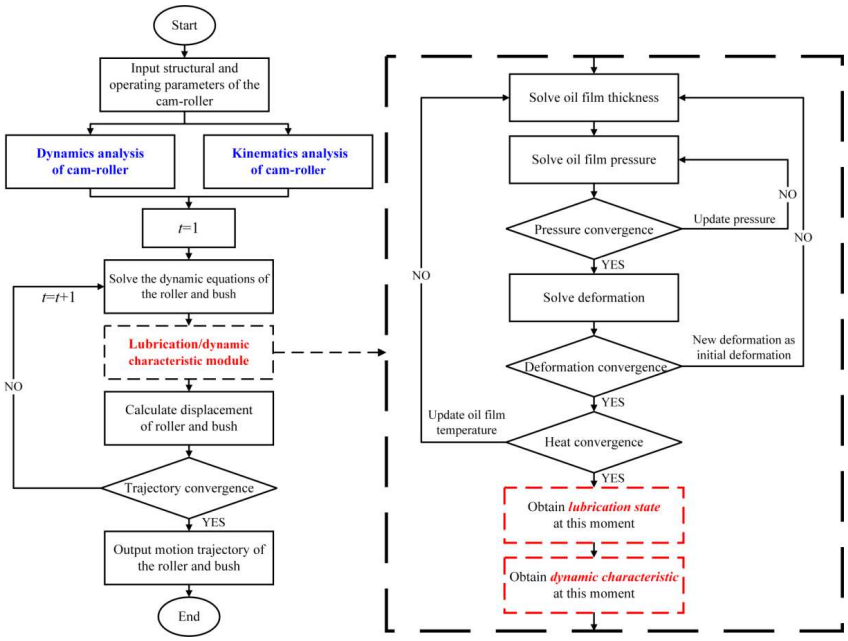

Fig.5. Flow chart of numerical analysis for thermoelastic hydrodynamic lubrication of the RFBP structure.

2.5 Verification of the lubrication/dynamic characteristics model

In order to verify the reliability of the double-layer oil film transient lubrication model, an experimental platform was built to test the speed of the floating bush. The structural diagram of the experimental platform is shown in Fig.6. The camshaft is driven to rotate by a servo motor (4.5kW power), and the cam drives the roller to rotate. The RFBP structure is loaded with springs, and the diameter of the springs is 6.0mm. The torque sensor (DYN-200) was used to measure the speed of the floating bush. The testing method involved fixing a gear to the side of the floating bush and meshing it with the sensor gear. The gear transmission is used to output the time-varying speed of the floating bush. The cam profile and lift curve used in the experiment are shown in Fig.7.

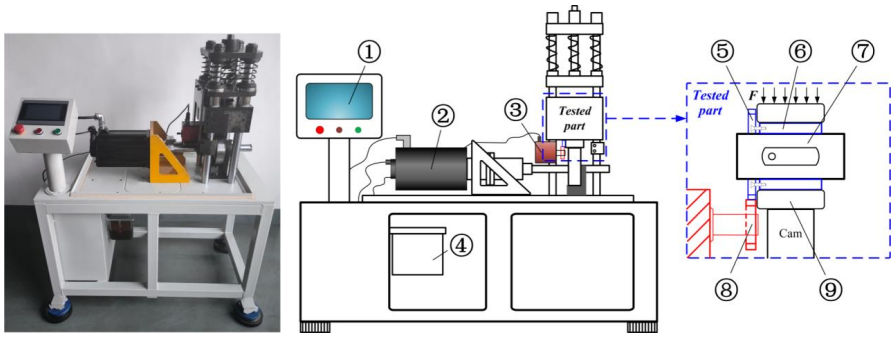

Fig.6. Test bench structure diagram.

1. Display screen 2. Electric motor 3. Speed Sensor 4. Oil tank 5. Floating bush gear 6. Floating bush 7. Roller pin 8. Sensor gear 9. Roller

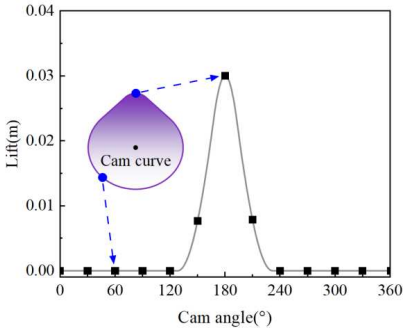

Fig.7. Cam profile and lift curve in the test.

The comparison results are shown in Fig.8. The comparison results of the average speed of the floating bush at different cam speeds are shown Fig.8(a). The average speed of the floating bush within the cycle is expressed by $\bar{\omega}_f$. The calculated results and tested results both increase with the cam speed, and the deviation is within 6%. Fig.8(b) shows that the instant speed comparison results of the floating bush. The calculated results of the floating bush speed variation trend with the cam angle are closely matches the tested results, and the numerical deviation of no more than 10%. In addition, the tested results are larger than the calculated results due to the oil holes around the floating bush in the test, a factor which is not considered in the simulation model [34]. The accuracy of the simulation model's calculation results is proved by the verification results.

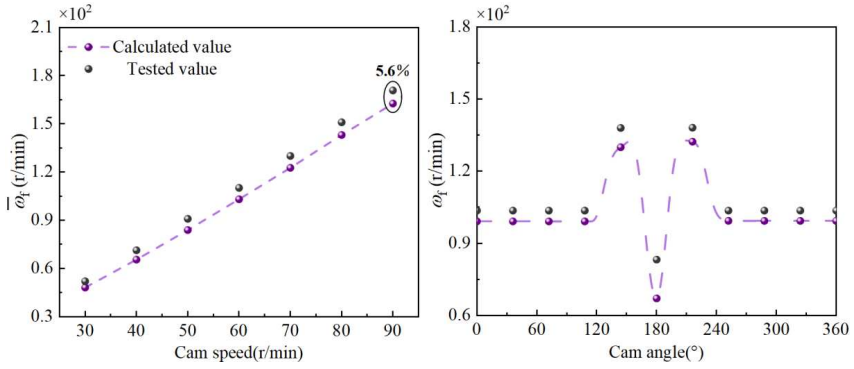

(a) (b)

Fig.8. Verification results of floating bush speed.
(a) Comparison results (average speed) (b) Comparison results(ω_1=60r/min).

In order to verify the accuracy of the calculation model of dynamic characteristic parameters, the single-layer oil film simulation model which is the degradation model of this work, was compared with the calculation results in the published studies [39]. The comparison results are shown in Fig.9. It can be observed that the trend of the two results is basically consistent, that is, as the eccentricity increases, the oil film's stiffness/damping parameters exhibit increase trend. The deviation between the two is within 8%, indicating the accuracy of the oil film dynamic characteristic model in this work.

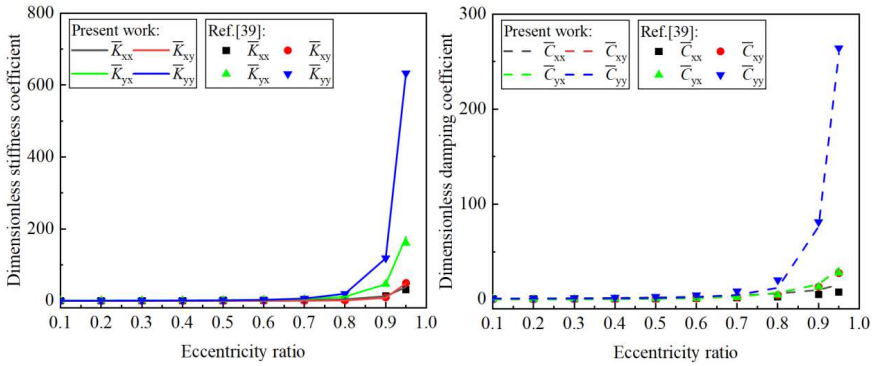

(a) (b)

Fig.9. Verification results of the dynamic characteristic parameters.
(a) Variation of dimensionless stiffness coefficient; (b) Variation of dimensionless damping coefficient.

In addition, the calculation is carried out under stable working conditions to verify grid independence of the model and the verification results are shown in Fig.10. The external load is taken

as 10000N and the roller speed is taken as 1000r/min. Fig.10(a) and (b) show circumferential and axial interface pressure distribution of RFBP of the maximum oil film pressure, respectively. Fig.10(a) and (b) are used to verify circumferential and axial grid independence, respectively. It can be found that when the number of circumferential and axial grids is small, the calculated oil film pressure distribution is not smooth enough, but the number of circumferential and axial grids have little effect on the maximum oil film pressure. Therefore, in order to describe the lubrication state of RFBP structure in more detail, and reduce the calculation time to a certain extent, 120×12 grid is selected.

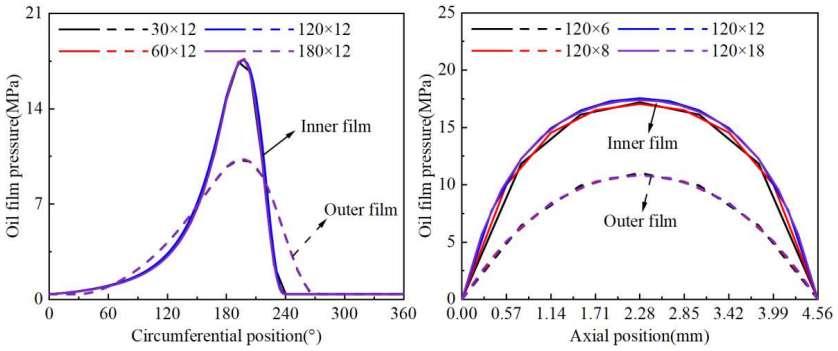

(a) (b)

Fig.10. The verification of the independence of the grid.
(a) Verification of circumferential grid independence; (b) Verification of axial grid independence.

The verification of the independence of the disturbance amount for the small disturbance method is as follows. The verification of the independence of the disturbance amount is shown in Fig.11. The stable operating conditions is used and the eccentricity of the outer oil film is controlled at 0.6. Due to the larger eccentricity of the inner oil film, the influence of disturbance on the oil film pressure is more significant[34]. Therefore, the stiffness and damping coefficient of the inner oil film are selected as the standard judgment for verifying the disturbance independence. It can be observed that as the disturbance displacement decreases from 1.5μm to 0.1μm, the inner film dimensionless stiffness coefficient shows a trend of first decreasing (1.5μm-1.0μm) and then reaching stability (1.0μm-0.1μm); The disturbance velocity is within the range of 0.015-0.001 times of ω_f, and the dimensionless damping remains almost unchanged. Based on the above results, the disturbance displacement is selected as 1.0μm, and the disturbance velocity is selected as 0.01 times ω_f.

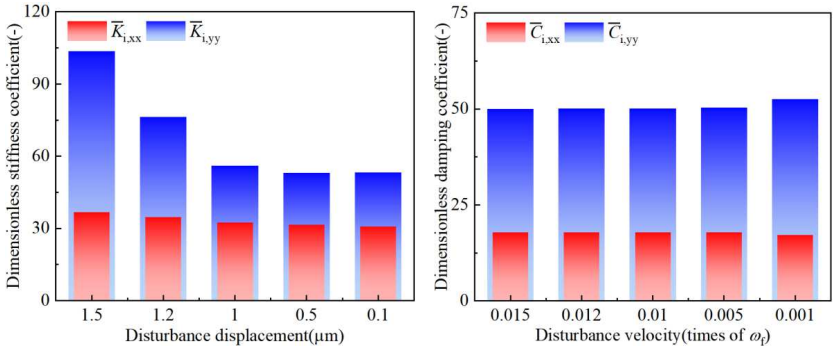

(a) (b)

Fig.11. The verification of the independence of the disturbance amount.
(a) Dimensional stiffness of inner oil film; (b) Dimensional damping of inner oil film.

3. Result analysis and discussion

Table 1 shows the calculation parameters of the dynamic characteristics of RFBP structure.

Table 1 Calculation parameters of dynamic characteristics of RFBP structure.

Project	Parameter
Cam base circle radius	65mm
Outer radius of the roller	40mm
Spring pre tightening force	200N
Spring stiffness	56.7N/mm
Outer radius of bush	24mm
Inner radius of bush	19mm
Bush length	45.6mm
Inner layer clearance	16μm
Outer layer clearance	20μm
Oil inlet temperature	65℃
Oil density	871kg/m^3

3.1 Analysis of cam-roller model

The result analysis of cam roller is shown in Fig.12. It is worth noting that in order to express more clearly, the special points have been taken at cam angles of 0°, 60°, 120°, 180°, 270°, and 360° in the figure. The variation curves of lift and pressure angle of the cam mechanism with the cam angle are shown in Fig.12(a). Peak lift is observed at about 60° cam angle, and the return section is completed at about 240°. The maximum pressure angle occurs within the range of 0-60° of the cam angle. Vertical motion properties (velocity/acceleration) of the roller are illustrated in Fig.12(b),

showing great variations across the 0-60° rotation range. The variation of the roller speed and comprehensive curvature radius with the cam angle are shown in Fig.10(c). It's clearly that the position of the maximum roller speed is nearly the same as the position of the maximum comprehensive curvature radius. The variation of fuel pressure and the sum of inertia and spring force with cam angle are shown in Fig.12(d). It is clearly that the fuel pressure value is much higher than the sum of inertia and spring forces, indicating that the main load on the roller comes from the fuel pressure. When the cam angle is about 60°, the fuel pressure reaches the peak, about 39.36MPa.

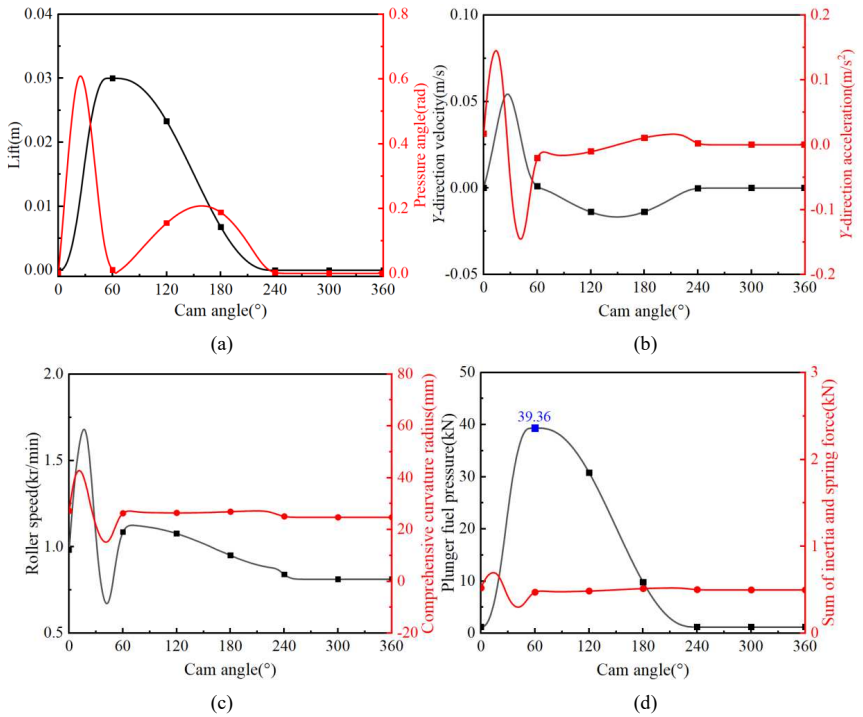

Fig.12. Verification results of the dynamic characteristic parameters. (a) The variation of the lift and pressure angle with cam angle; (b) The variation of *y*-direction velocity and acceleration with cam angle; (c) The variation of comprehensive curvature radius and roller speed with cam angle; (d) The variation of fuel pressure and the sum of inertia and spring force with cam angle.

3.2 Analysis of dynamic characteristics of inner/outer film

Fig.13 shows the analysis results of the lubrication characteristics of RFBP structure. and Fig.12(a) shows the variation curve of the maximum oil film pressure of the inner and outer layers

($p_{i,max}$, $p_{o,max}$) with the cam angle. The point-M and point-N in the Fig.13(a) represent the extreme values of $p_{i,max}$ and $p_{o,max}$ within the cycle, respectively. And the distribution of oil film pressure at point-M and point-N are also shown in Fig.13(a). It can be found that $p_{i,max}$ is larger than $p_{o,max}$, which is due to the smaller inner layer structure and poor load-bearing capacity. In addition, the inner layer has a smaller oil film bearing area compared to the outer layer. The trend of relative speed of the inner/outer layers of the floating bush with the cam angle are shown in Fig.13(b). It is apparent that the relative speed of the outer layer changes significantly compared to the inner layer. The relative displacement changes of floating bush and roller along x/y axes are depicted in Fig.13(c) and (d). The relative displacement of the floating bush is the displacement of the floating bush center O_f which is relative to the roller pin center O_p, and the relative displacement of the roller is the displacement of the roller center O_2 which is relative to the floating bush center O_f. It can be observed that the maximum distance between O_f and O_p in the x-direction occurs at a cam angle of about 300°, which is about 12.2μm. The maximum distance between O_f and O_p in the y-direction occurs at a cam angle of about 120°, which is about 12.5μm. In addition, the peak distance in the x-direction between O_2 and O_f occurs at a cam angle of about 210°, which is about 11.2μm. The peak distance in the y-direction between O_2 and O_f occurs at a cam angle of about 60°,which is about 12.3μm.

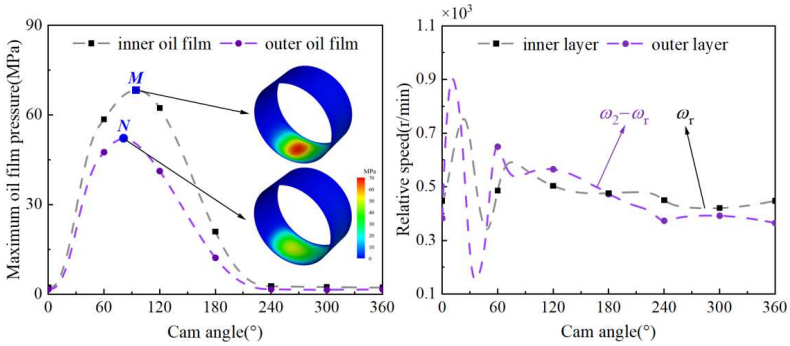

(a) (b)

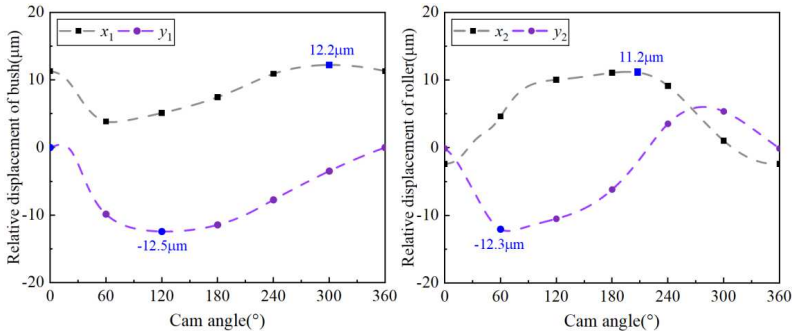

(c) (d)

Fig.13. Analysis of lubrication characteristics of RFBP structure. (a) The variation of $p_{i,max}$ and $p_{o,max}$ with cam angle; (b) The relative speed of the inner and outer layers varies with the cam angle; (c) The variation of relative displacement of floating bush with cam angle; (d) The variation of relative displacement of roller with cam angle.

Fig.14 presents the evolution of dimensionless stiffness/damping coefficients as the cam angle changes. Since the main stiffness/damping coefficients have a greater impact on the dynamic performance of equipment structure compared to the cross stiffness/damping coefficients, and the variation law with eccentricity is similar, the work uses main stiffness/damping coefficients to perform a parametric analysis [36]. The variation curves of the dimensionless main stiffness/damping coefficients of the inner film with the cam angle are shown in Fig.14(a) and (b). The peak values of the inner main stiffness along the *x*- and *y*-axes are about 43.3 and 86.8, attained at cam angles about 270° and 150°, respectively. The main stiffness variations along the *x*-axis during cam rotation correlate with the oil film's relative displacement changes in the corresponding direction, while an analogous relationship is observed for the *y*-axis components. This phenomenon occurs because oil film stiffness and damping coefficients increase with rising eccentricity [39]. The key reason is that at high eccentricity, oil film pressure responds more strongly to disturbances. Since the change of eccentricity represents the relative displacement change, the changes in stiffness and damping with cam angle relate directly to relative displacement. The variation curves of the dimensionless main stiffness/damping coefficients of the outer film with the cam angle are shown in Fig.14(c) and (d). It can be observed that the stiffness/damping coefficients of the outer oil film are smaller than those of the inner oil film, and similar to the inner oil film, the trend of change with cam angle is related to relative displacement. The variation curves of the equivalent stiffness/damping coefficients with the cam angle are shown in Fig.14(e) and (f). It can be seen that the equivalent main stiffness/damping

coefficients of the RFBP structure is smaller than the stiffness/damping coefficients of both the inner and outer films. Therefore, the double-layer oil film structure can reduce the stiffness/damping of the structure contrasted with the single-layer oil film structure. In addition, due to the series relationship between the inner and outer oil films, the dynamic coefficients of the inner and outer oil films follow the series principle of springs. According to the basic mathematical relationship of equivalent stiffness/damping coefficients with the those of the inner and outer films (equations (24) and (25)), it indicates that the outer oil film's main stiffness/damping coefficients has a more pronounced influence on the equivalent stiffness/damping coefficients compared to inner counterpart.

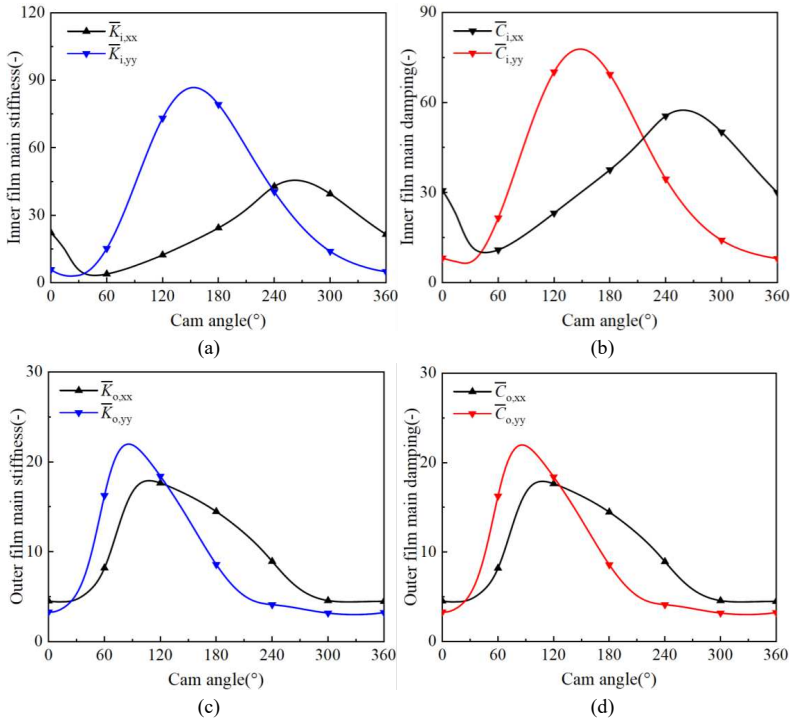

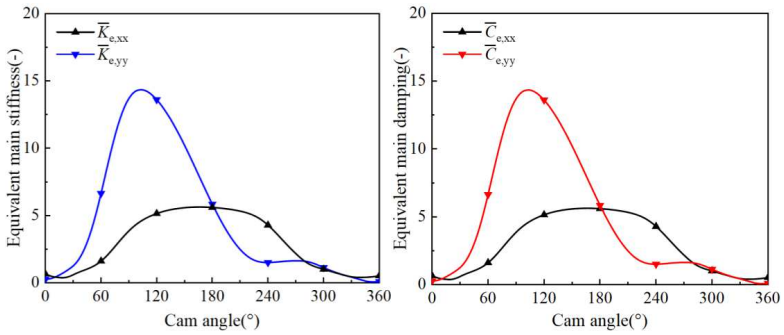

(e) (f)

Fig.14. The variation of dimensionless stiffness/damping coefficients with cam angle. (a) The variation of inner film dimensionless main stiffness with cam angle; (b) The variation of inner film dimensionless main damping with cam angle; (c) The variation of outer film dimensionless main stiffness with cam angle; (d) The variation of outer film dimensionless main damping with cam angle; (e) The variation of dimensionless equivalent main stiffness with cam angle; (f) The variation of dimensionless equivalent main damping with cam angle.

3.3 The use of RFBP dynamic characteristics in camshaft bending vibration

Based on ANAYS APDL simulation analysis, the dynamic characteristics of the RFBP structure calculated in this paper are included in the camshaft bending vibration model. The dynamic characteristics of RFBP structure are associated with the dynamic characteristics at the cam-roller to obtain the support boundaries of each gear cam. In addition, the RFBP structure oil film and the cam-roller oil film are in series, and the oil film stiffness and damping coefficient between the cam and roller is taken as 10^9 and 10^7, respectively. The current work analyzes a diesel engine fuel supply camshaft (Fig.15) with six cams (C_1-C_6). Pairs (C_1, C_6), (C_2, C_5), and (C_3, C_4) share consistent fuel supply tim**es.** Fig.16 shows the camshaft's bending vibration characteristics The first fifteen natural frequencies are shown in Fig.16(a), and the displacement at each cam center in Fig.16(b). It can be observed that as the fuel supply timing of the cam is consistent, the maximum displacement time of bending vibration is also close.

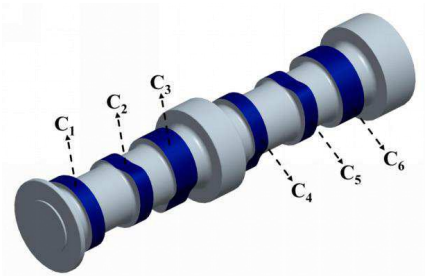

Fig.15. The geometric model of fuel pump camshaft.

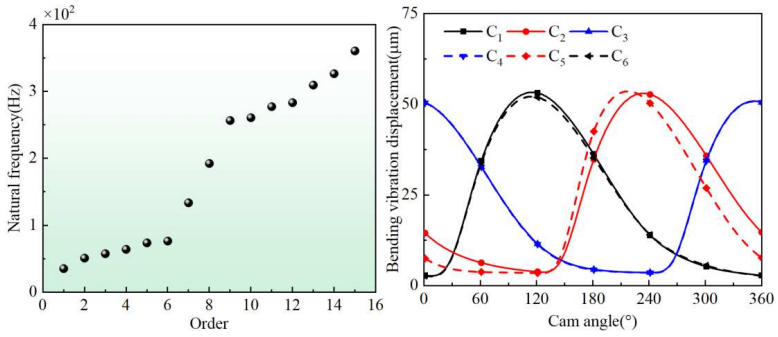

(a) (b)

Fig.16. The bending vibration characteristics of camshaft

(a) The first fifteen natural frequencies; (b) the displacement at each cam center.

3.4 The effect of operating parameters

3.4.1 The effect of cam speed

Fig.17 shows the relative motion trajectories of the floating bush and roller as the cam speed (ω_1) varies. Fig.17(a) and (b) show the relative motion trajectory of the floating bush and roller, respectively. It can be discovered that as the cam speed increases, the relative motion trajectories of the floating bush and roller both move to the top left. As a consequence, the eccentricity of the inner/outer oil films decrease, and this is due to the dynamic pressure effect, which enhances the bearing capacity of the oil films.

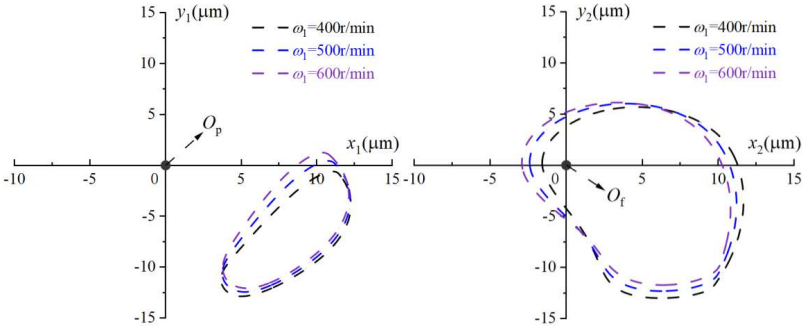

(a) (b)

Fig.17. The effect of cam speed on the relative motion trajectories of floating bush and roller (Cam speed is set to 400r/min, 500r/min and 600r/min). (a) Relative motion trajectory of floating bush (b) Relative motion trajectory of roller.

Fig.18 shows the effect of cam speed on the dimensionless main stiffness/damping coefficients

of the inner/outer films. Fig.18(a) and (b) depict the variations of dimensionless main stiffness along the *x*- and *y*-axes with the cam angle. It can be found that as the cam speed increases, the stiffness of the inner/outer films decreases, which is due to the decrease the inner/outer films' eccentricity. It can also be seen that, when the cam speed increases, the stiffness of the inner film decreases more significantly compared to the stiffness of the outer film. The reason is that the inner film structure is smaller, the lubrication properties of the inner film are more sensitive to variations in cam speed compared to the outer film [34]. Fig.18(c) and (d) depict the variations of dimensionless main damping components along the *x*- and *y*-axes with the cam angle. It can be found that, similar to the stiffness of the oil film, when the cam speed increases, the damping of the inner/outer films decreases, and the damping of inner film changes more significantly compared to the damping of the outer film.

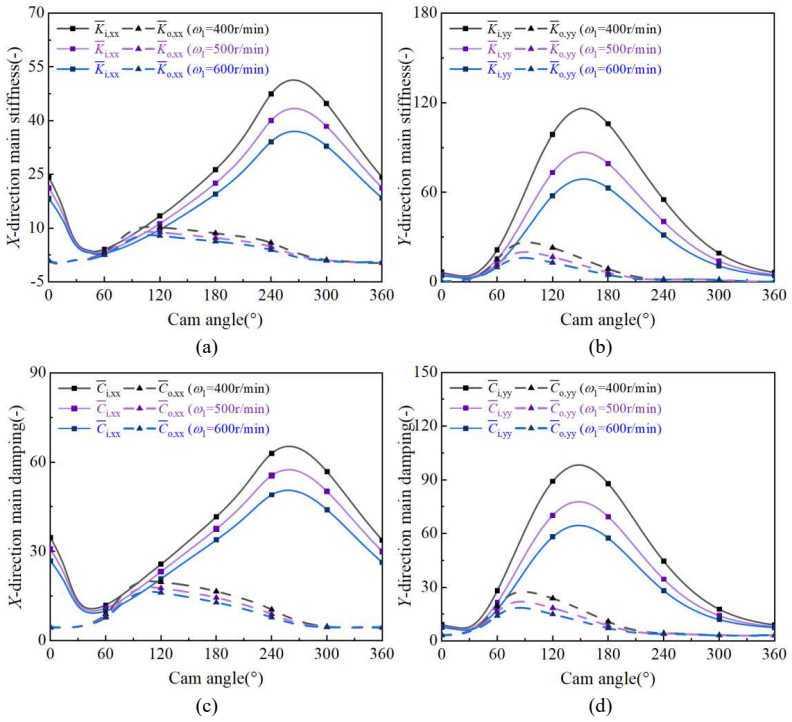

Fig.18. The effect of cam speed on the dimensionless main stiffness/damping coefficients of the inner/outer oil film (Cam speed is set to 400r/min, 500r/min and 600r/min). (a) The variation of *x*-direction dimensionless main stiffness with cam angle; (b) The variation of *y*-direction dimensionless main stiffness with cam angle; (c) The variation of *x*-direction dimensionless main damping with cam angle; (d) The variation of *y*-direction dimensionless main damping with cam angle.

Fig.19 shows the effect of cam speed on the dimensionless equivalent main stiffness/damping coefficients of RFBP structure. Fig.19(a) and (b) show the dimensionless equivalent main stiffness and damping coefficients with the variation of cam angle, respectively. Fig.19(c) and (d) show the peak values of dimensionless equivalent main stiffness and damping (the peak value of $\overline{K}_{e}$ and $\overline{C}_{e,}$) at varying cam speeds. It can be seen that as the cam speed increases, both the dimensionless equivalent main stiffness and damping coefficients decrease. In addition, *y*-direction dynamics characteristics are more sensitive to cam speed changes than *x*-direction dynamics characteristics. When the cam speed increases from 400r/min to 600r/min, the peak value of $\overline{K}_{e}$ and $\overline{C}_{e}$ in the *y*-direction decrease more significantly ($\overline{K}_{e,yy}$ decreases by 42%, $\overline{C}_{e,yy}$ decreases by 35%) compared to the decrease in the *x*-direction ($\overline{K}_{e,xx}$ decreases by 29%, $\overline{C}_{e,xx}$ decreases by 22%).

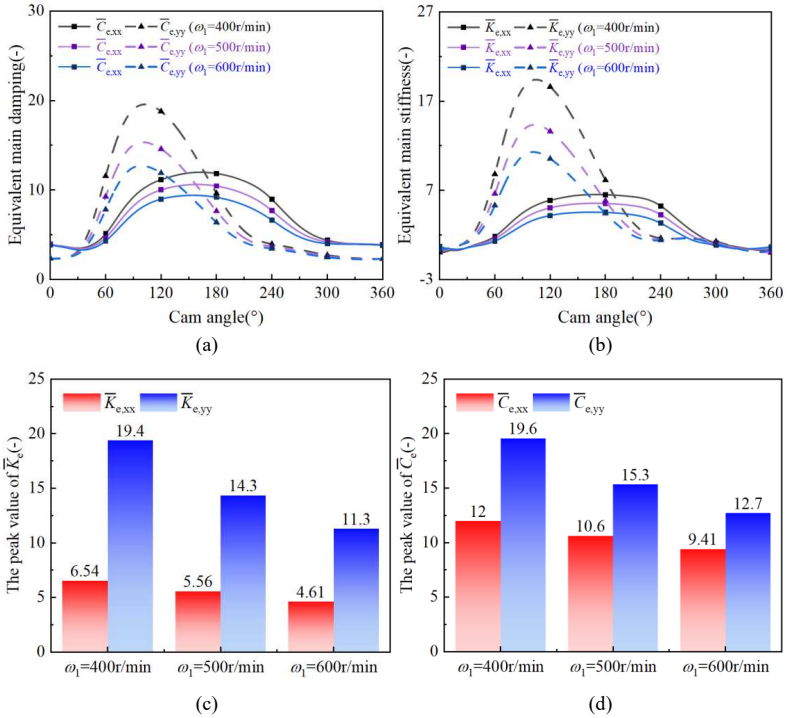

Fig.19. The effect of cam speed on the dimensionless equivalent stiffness/damping coefficients (Cam speed is set to 400r/min, 500r/min and 600r/min). (a) The variation of dimensionless equivalent main stiffness with cam angle; (b) The variation of dimensionless equivalent main damping with cam angle; (c) The peak value of dimensionless equivalent main stiffness; (d) The peak value of dimensionless equivalent main damping.

3.4.2 The effect of fuel pressure

Fig.20 shows the relative motion trajectories of the floating bush and roller as the fuel pressure varies. Fig.20(a) and (b) show the relative motion trajectory of the floating bush and roller, respectively. The work adjusts the maximum fuel pressure (p_2) to change the fuel pressure. It can be observed that the relative motion trajectories of the floating bush and roller both tend to move to the lower right, which elevates eccentricity levels in both inner and outer films. The reason is that as the fuel pressure increases, the external load on the RFBP structure increases.

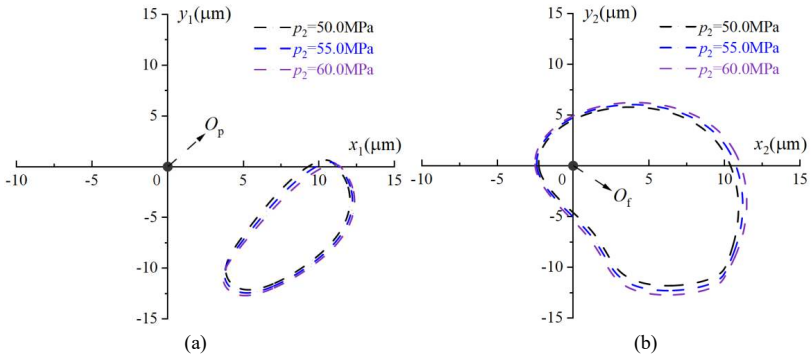

Fig.20. The effect of fuel pressure on the relative motion trajectories of roller and floating bush (Fuel pressure is set to 50.0MPa, 55.0MPa and 60.0MPa) (a) Relative motion trajectory of floating bush (b) Relative motion trajectory of roller

Fig.21 shows the effect of fuel pressure on the dimensionless main stiffness/damping coefficients of the inner/outer oil films. Fig.21(a) and (b) illustrate the variations in dimensionless main stiffness along the *x*- and *y*-axes with the cam angle. It can be found that as the fuel pressure increases, the stiffness of the inner/outer oil film increase, as a result of the oil films eccentricity increase. Moreover, when the fuel pressure increases, the stiffness of the inner oil film increases more significantly. Fig.21(c) and (d) illustrate the variations in dimensionless main damping properties along the *x*- and *y*-axes with the cam angle. It can be found that, similar to the stiffness of the oil film, when the fuel pressure increases, the damping of the inner/outer films decreases. And when the fuel pressure increases, the inner film damping changes more significantly.

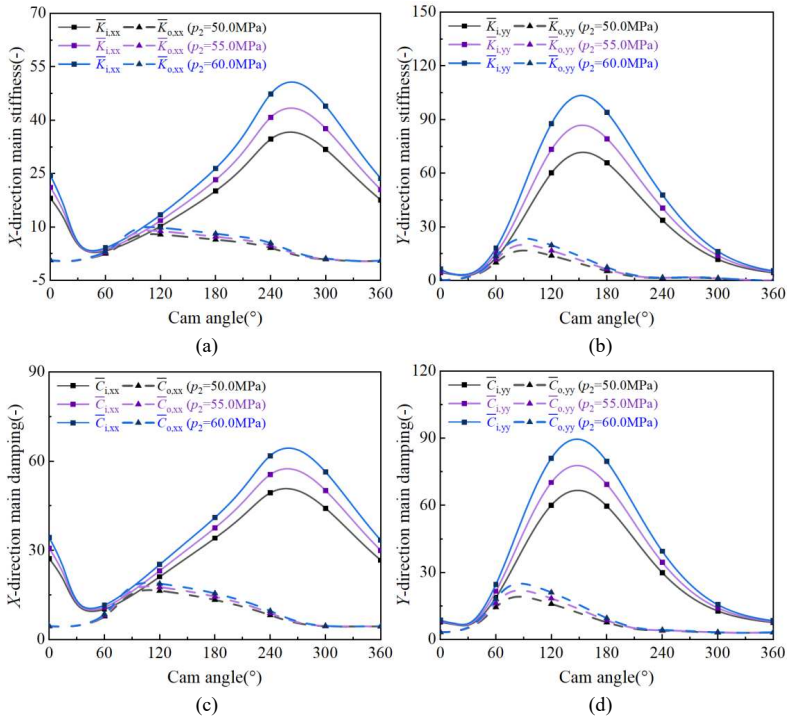

Fig.21. The effect of fuel pressure on the dimensionless main stiffness/damping coefficients of inner/outer oil film (Fuel pressure is set to 50.0MPa, 55.0MPa and 60.0MPa). (a) The variation of *x*-direction dimensionless main stiffness with cam angle; (b) The variation of *y*-direction dimensionless main stiffness with cam angle; (c) The variation of *x*-direction dimensionless main damping with cam angle; (d) The variation of *y*-direction dimensionless main damping with cam angle.

Fig.22 shows the effect of fuel pressure on the dimensionless equivalent main stiffness/damping coefficients of RFBP structure. Fig.22(a) and (b) show the dimensionless equivalent main stiffness and damping coefficients with the variation of cam angle, respectively. Fig.21(c) and (d) show the peak values of dimensionless equivalent main stiffness and damping at varying fuel pressure. It can be seen that as the fuel pressure increases, the higher fuel pressure enhanced equivalent stiffness and damping values. In addition, *y*-direction dynamics characteristics are more sensitive to fuel pressure changes than *x*-direction dynamics characteristics. When the fuel pressure increases from 50.0MPa to 60.0MPa, the peak value of $\overline{K}_e$ and $\overline{C}_e$ in the *y*-direction increase more significantly ($\overline{K}_{e,yy}$ increases by 42.8%, $\overline{C}_{e,yy}$ increases by 32.3%) compared to the increase in the *x*-direction ($\overline{K}_{e,xx}$ increases by 21.7%, $\overline{C}_{e,xx}$ increases by 15.7%).

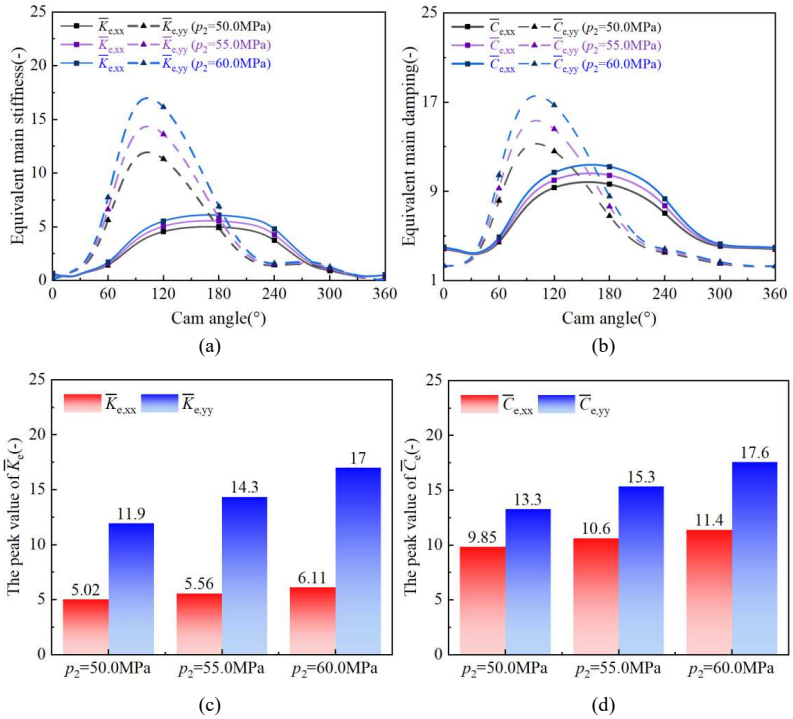

Fig.22. The effect of fuel pressure on the dimensionless equivalent stiffness/damping coefficients (Fuel pressure is set to 50.0MPa, 55.0MPa and 60.0MPa). (a) The variation of dimensionless equivalent main stiffness with cam angle; (b) The variation of dimensionless equivalent main damping with cam angle; (c) The peak value of dimensionless equivalent main stiffness; (d) The peak value of dimensionless equivalent main damping.

3.5 The effect of structural parameters

3.5.1 The effect of aspect ratio

Fig.23 shows the relative motion trajectories of the roller and the floating bush as the floating bush aspect ratio (L/D value) varies. Fig.23(a) and (b) show the relative motion trajectory of the floating bush and roller, respectively. The work controls the floating bush aspect ratio by changing the width of the floating bush. An increase in the L/D value causes a shift of both the roller and floating bush's relative motion trajectories tend to move to top left, resulting in a decrease in the eccentricity of the inner/outer oil films. The reason is that the increase in aspect ratio enhances the load-bearing capacity of the inner/outer oil films.

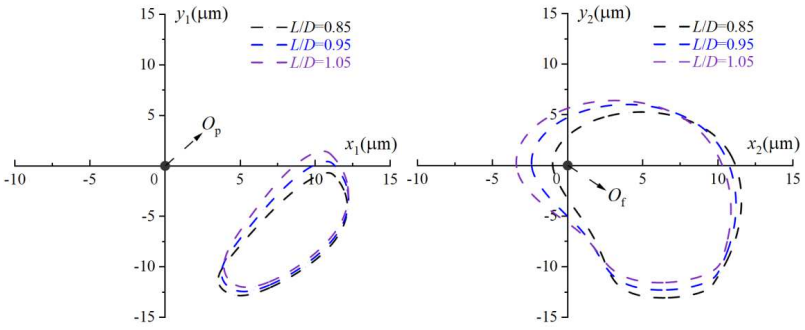

Fig.23. The effect of aspect ratio on the relative motion trajectories of roller and floating bush (Aspect ratio is set to 0.85, 0.95 and 1.05). (a) Relative motion trajectory of floating bush (b) Relative motion trajectory of roller.

Fig.24 shows the effect of the *L*/*D* value on the dimensionless main stiffness/damping coefficients of the inner/outer oil film. Fig.24(a) and (b) illustrate the variations in dimensionless main stiffness along the *x*- and *y*-axes with the cam angle. It can be found that as the *L*/*D* value increases, the stiffness of the inner/outer oil film decreases, as a result of the oil film eccentricity decreases. Moreover, when the *L*/*D* value increases, the stiffness of the inner oil film decreases more significantly. Fig.24(c) and (d) illustrate the variations in dimensionless main damping along the *x*- and *y*-axes with the cam angle. It can be found that, similar to the oil film stiffness, when the *L*/*D* value increases, the inner/outer oil film damping decreases, and the inner oil film damping changes more significantly.

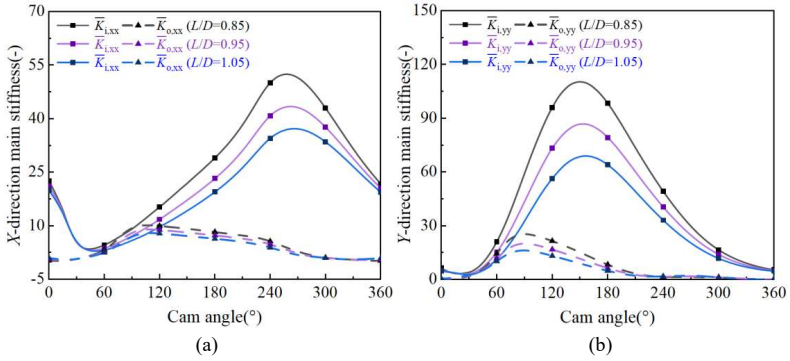

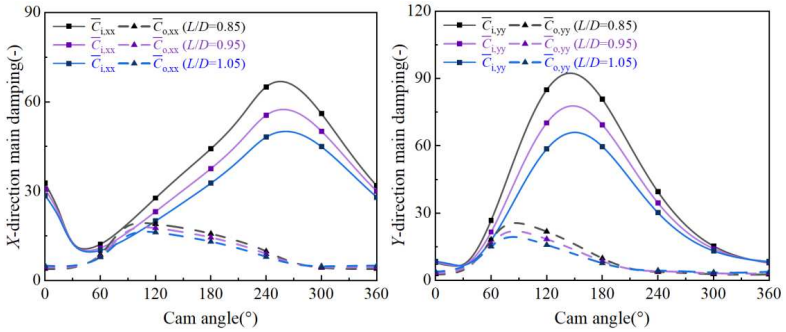

Fig.24. The effect of aspect ratio on the dimensionless main stiffness/damping coefficients of the inner/outer oil film (Aspect ratio is set to 0.85, 0.95 and 1.05). (a) The variation of *x*-direction dimensionless main stiffness with cam angle; (b) The variation of *y*-direction dimensionless main stiffness with cam angle; (c) The variation of *x*-direction dimensionless main damping with cam angle; (d) The variation of *y*-direction dimensionless main damping with cam angle.

Fig.25 shows the effect of *L*/*D* value on the dimensionless equivalent main stiffness/damping coefficients of RFBP structure. Fig.25(a) and (b) show the dimensionless equivalent main stiffness and damping coefficients with the variation of cam angle, respectively. Fig.25(c) and (d) show the peak values of dimensionless equivalent main stiffness and damping at varying *L*/*D* value. It can be seen that as the *L*/*D* value increases. In addition, *y*-direction dynamics characteristics are more sensitive to *L*/*D* value changes than *x*-direction dynamics characteristics. When the *L*/*D* value increases from 0.85 to 1,05, the peak value of $\overline{K}_e$ and $\overline{C}_e$ in the *y*-direction decrease more significantly ($\overline{K}_{e,yy}$ decreases by 38.1%, $\overline{C}_{e,yy}$ decreases by 28.9%) compared to the decrease in the *x*-direction ($\overline{K}_{e,xx}$ decreases by 27.5%, $\overline{C}_{e,xx}$ decreases by 19.2%).

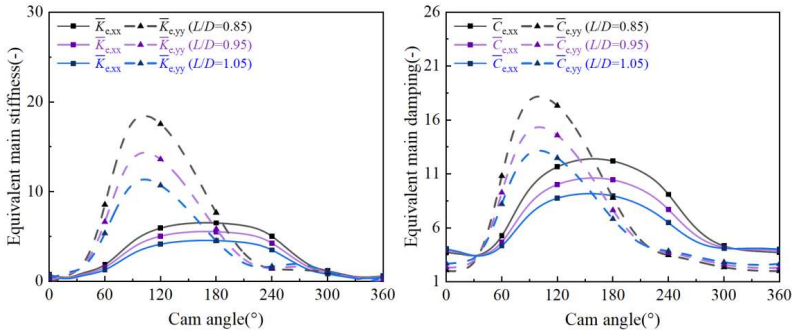

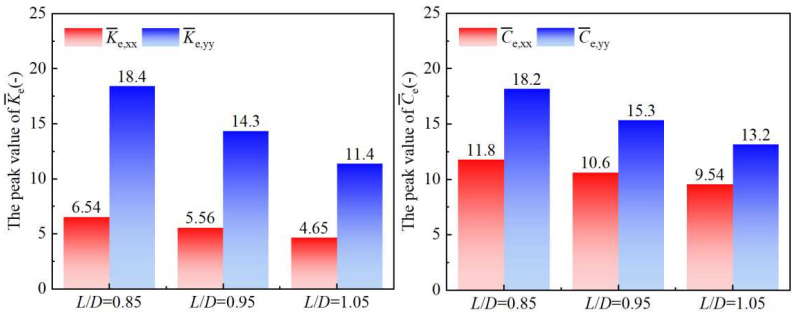

(c) (d)

Fig.25. The effect of aspect ratio on the dimensionless equivalent stiffness/damping coefficients (Aspect ratio is set to 0.85, 0.95 and 1.05). (a) The variation of dimensionless equivalent main stiffness with cam angle; (b) The variation of dimensionless equivalent main damping with cam angle; (c) The peak value of dimensionless equivalent main stiffness; (d) The peak value of dimensionless equivalent main damping.

3.5.2 The effect of clearance ratio

Fig.26 shows the relative motion trajectories of the floating bush and roller as the clearance ratio (c_i/c_o value) varies. Fig.26(a) and (b) show the relative motion trajectory of the floating bush and roller, respectively. The c_i/c_o value is adjusted by fixing the outer clearance and changing the inner clearance. It can be observed that as the c_i/c_o value increases, the relative motion trajectory moves downward to the left, as a result, the eccentricity of the inner oil film increases. The reason is that the inner film bearing capacity decreases which is caused by the higher c_i/c_o value. And due to the inner clearance increases, the range of motion of the floating bush increases. In addition, because the outer clearance remains unchanged, the load-bearing capacity of the outer oil film and the relative motion trajectory of the rollers also remain essentially unchanged.

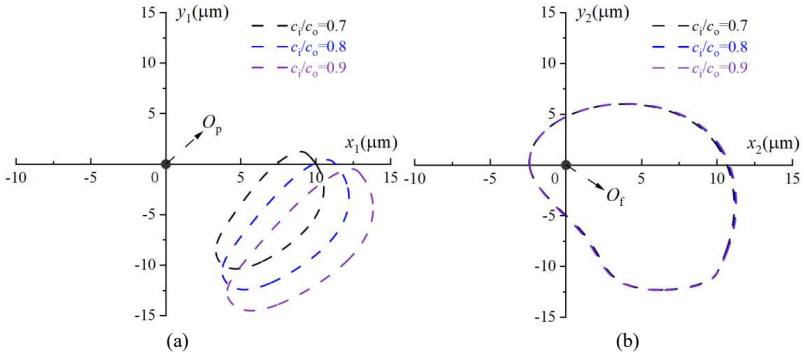

(a) (b)

Fig.26. The effect of clearance ratio on the relative motion trajectories of roller and floating bush (Clearance ratio

is set to 0.7, 0.8 and 0.9). (a) Relative motion trajectory of floating bush (b) Relative motion trajectory of roller.

Fig.27 shows the effect of the c_i/c_o value on the dimensionless main stiffness/damping coefficients of the inner/outer oil film. Fig.27(a) and (b) illustrate the variations in dimensionless main stiffness along the *x*- and *y*-axes with the cam angle. It can be found that as the c_i/c_o value increases, the stiffness of the inner oil film increases, and the stiffness of the outer oil film remains basically unchanged. The reason for this is that as the c_i/c_o value increases, the load-bearing capacity of the inner layer becomes weak and the outer layer remains basically unchanged. Fig.27(c) and (d) illustrate the variations in dimensionless main damping along the *x*- and *y*-axes with the cam angle. It can be found that, similar to the oil film stiffness, when the c_i/c_o value increases, the inner oil film damping increases, and the outer oil film damping remains basically unchanged.

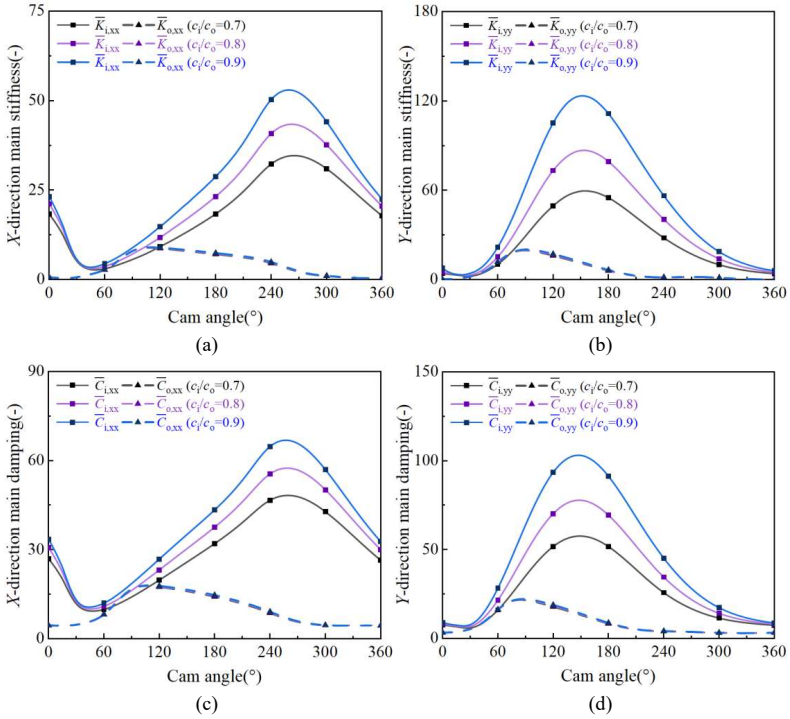

Fig.27. The effect of clearance ratio on the dimensionless main stiffness/damping coefficients of the inner/outer oil film (Clearance ratio is set to 0.7, 0.8 and 0.9). (a) The variation of *x*-direction dimensionless main stiffness with cam angle; (b) The variation of *y*-direction dimensionless main stiffness with cam angle; (c) The variation of *x*-direction dimensionless main damping with cam angle; (d) The variation of *y*-direction dimensionless main damping with cam angle.

Fig.28 shows the effect of c_i/c_o value on the dimensionless equivalent main stiffness/damping coefficients of RFBP structure. Fig.28(a) and (b) show the dimensionless equivalent main stiffness and damping coefficients with the variation of cam angle, respectively. Fig.28(c) and (d) show the peak values of dimensionless equivalent main stiffness and damping at varying c_i/c_o value. It can be seen that as the c_i/c_o value increases, the dimensionless equivalent main stiffness/damping coefficients increase. In addition, *y*-direction dynamics characteristics are more sensitive to fuel pressure changes than *x*-direction dynamics characteristics. When the c_i/c_o value increases from 0.7 to 0.9, the peak value of $\overline{K}_e$ and $\overline{C}_e$ in the *y*-direction increase more significantly ($\overline{K}_{e,yy}$ increases by 36.9%, $\overline{C}_{e,yy}$ increases by 25.9%) compared to the increase in the *x*-direction ($\overline{K}_{e,xx}$ increases by 32.8%, $\overline{C}_{e,xx}$ increases by 18.8%).

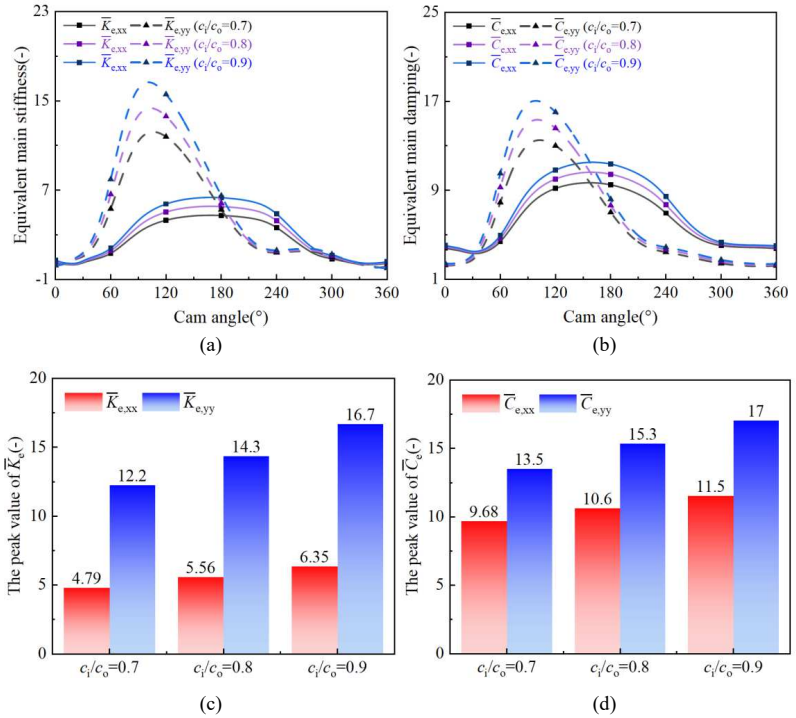

Fig.28. The effect of clearance ratio on the dimensionless equivalent stiffness/damping coefficients (Clearance ratio is set to 0.7, 0.8 and 0.9). (a) The variation of dimensionless equivalent main stiffness with cam angle; (b) The variation of dimensionless equivalent main damping with cam angle; (c) The peak value of dimensionless equivalent main stiffness; (d) The peak value of dimensionless equivalent main damping.

Conclusions

This work established a transient dynamic property calculation model for RFBP structure, where the cam-roller dynamics and kinematic behaviors were considered. The test bed was designed to simulate the operation of real RFBP structure, and the calculated results showed strong correlation with the test results. The deviation between test and calculated results is no more than 10%, which confirms the accuracy of the calculated results. The dynamic properties of the inner/outer films were compared, and the effect of structural and operating parameters on the dynamic characteristic of the structure were analyzed, and the dynamic characteristics of RFBP structure were used to calculate the preliminary analysis of camshaft vibration. Primary research outcomes are outlined below:

The inner film demonstrates inferior lubrication performance compared to the outer film, while exhibiting higher stiffness and damping properties, and the equivalent stiffness/damping of the RFBP structure are smaller compared to the two. The double-layer oil film structure can greatly increase the structural elasticity. The dynamic characteristics of the outer film have a more significant impact on the equivalent dynamic characteristics of the RFBP structure. More attention should be paid to the outer oil film in the structural dynamic performance design of high-pressure fuel pump RFBP. The main stiffness/damping of the inner film varying with the cam angle is related to the relative displacement of the floating bush. The main stiffness/damping of the outer film varies with the cam angle is related to the relative displacement of the roller. In addition, the series relationship between the dynamic characteristics of the RFBP structure and the cam-roller oil film dynamic characteristics was explained, and an example was proposed to illustrate the application of the RFBP structure dynamic characteristics of in camshaft vibration. However, how the dynamic characteristics of the RFBP affect the vibration response, and the bidirectional mapping relationship between vibration and lubrication, have not been analyzed.

Finally, some analysis was conducted on the transient dynamic characteristics under different operating conditions and structural parameters, and Some conclusions can be drawn. As the cam speed increases, the inner/outer films dynamic characteristic coefficients and equivalent dynamic properties coefficients of both decreases, and as the fuel pressure increases, the dynamic characteristic coefficients mentioned above increases. In addition, as the aspect ratio increases, the inner/outer films dynamic characteristic coefficients and equivalent dynamic characteristic coefficients both decreases. As the clearance ratio increases, both the inner oil film dynamic characteristic coefficients and the

equivalent dynamic characteristic coefficients increase, while the outer oil film dynamic characteristic coefficient remains basically unchanged. Since the dynamic characteristics of the RFBP structure is the boundary conditions for camshaft vibration, the research of dynamic characteristics under varying operating conditions and structural parameters can offer foundational guidance for camshaft vibrations in fuel pump. In addition, the studies can provide guidance for the design of dynamic characteristics of fuel pump RFBP structure.

Acknowledgement:

This work was supported by the National Natural Science Foundation of China (Grant No. 52271312 and 52475214) and Excellent Youth Foundation of Heilongjiang Province of China (Grant No. YQ2024E037).

References:

[1] Zheng L, Zhu H, Zhu J, Deng Y. Effects of oil film thickness and viscosity on the performance of misaligned journal bearings with couple stress lubricants[J]. Tribol Int 2020;146:106229.

[2] Ma J, Zhang H, Shi Z, Chu F, Gu F, et al. Modelling Acoustic Emissions induced by dynamic fluid-asperity shearing in hydrodynamic lubrication regime[J]. Tribol Int 2021; 153:106590.

[3] Xie Z, Jiao J, Yang K. A state-of-art review on the water-lubricated bearing[J]. Tribol Int 2023; 180:108276.

[4] Xie Z, Jiao J, Wrona S. The fluid-structure interaction lubrication performances of a novel bearing: experimental and numerical study[J]. Tribol Int 2023; 179:108151.

[5] Xie Z, Jiao J, Yang K. Experimental and numerical study on the mixed lubrication performances of a new bearing[J]. Tribol Int 2023; 182:108334.

[6] Soni S, Vakharia D. Dynamic performance analysis of a noncircular cylindrical floating ring bearing[J]. Proceedings of the Institution of Mechanical Engineers, Part J: Journal of Engineering Tribology,2017,231(6):745-765.

[7] Soni S, Vakharia D. A steady-state performance analysis of a non-circular cylindrical floating ring journal bearing[J]. Proceedings of the Institution of Mechanical Engineers, Part J: Journal of Engineering Tribology,2017,231(1):41-56.

[8] Pei S, Xu H, Yun M, et al. Effects of surface texture on the lubrication performance of the floating ring bearing[J]. Tribology International,2016,102.

[9] Yang Dequan, DAI Yujie. The Boundary Element Analysis of Stability in Dislocated Floating-ring Bearing [J]. Lubrication Engineerig, 2006, (01):38-40.

[10] Longkai W, Guangfu B, Xuejun L, et al. Effects of Floating Ring Bearing Manufacturing Tolerance Clearances on the Dynamic Characteristics for Turbocharger[J]. Chinese Journal of Mechanical Engineering, 2015,28(03):530-540.

[11] KANG Yang, QIU Zizhen, FAN Qiming, et al. Effect of the Number of Oil Holes on Lubrication Characters of Floating Ring Bearing[J]. Lubrication Engineerig,2023,48(09):83-90.

[12] Dong J ,Wen H ,Zhu J , et al. Analysis of Thermo-Hydrodynamic Lubrication of Three-Lobe Semi-Floating Ring Bearing Considering Temperature–Viscosity Effect and Static Pressure Flow[J].Lubricants,2024,12(4):140-.

[13] Andrés S L, Kerth J. Thermal effects on the performance of floating ring bearings for turbochargers[J]. Proceedings of the Institution of Mechanical Engineers, Part J: Journal of Engineering Tribology,2004,218(5).

[14] Holt C, San Andre S L, Sahay S, et al. Test Response and Nonlinear Analysis of a Turbocharger Supported on Floating Ring Bearings[J]. Journal of Vibration & Acoustics, 2005, 127(2):501-510.

[15] Andres S L, Rivadeneira C J, et al. Rotordynamics of Small Turbochargers Supported on Floating Ring Bearings- Highlights in Bearing Analysis and Experimental Validation[J]. Journal of Tribology,2007,129(2).

[16] Liqiang P, Lixin W, Zhiying Q, et al. Oil-film forming behavior of floating ring bearing under oil-starved lubrication[J]. Wear, 2023,524-525.

[17] Chao Q, Yang K, Kun S, et al. Effect of surface roughness on static characteristics of floating ring bearing[J]. Lubrication Engineering, 2017, 42(5): 66-72.

[18] P. Novotný, P. ˇ Skara, J. Hliník, The effective computational model of the hydrodynamics journal floating ring bearing for simulations of long transient regimes of turbocharger rotor dynamics [J], International Journal of Mechanical Sciences. 148 (2018) 611–619.

[19] Shuai Y, Junxing H, Xiaodong A, et al. Influence of floating ring elastic deformation on ring equilibrium and minimum film thickness for a hydrodynamic/hydrostatic floating ring bearing[J]. Industrial Lubrication and Tribology,2023,75(10):1178-1187.

[19] Zhao J, Gu Y, Yi S, et al. Influence of structural parameters of turbocharger floating bearing on

its dynamic characteristic coefficients[J]. Journal of Beijing Institute of Technology, 2017, 26(2): 183-190.

[21] Bin G, Huang Y, Guo S, et al.Investigation of Induced Unbalance Magnitude on Dynamic Characteristics of High-speed Turbocharger with Floating Ring Bearings[J].Chinese Journal of Mechanical Engineering,2018,31(1):88.

[22] Hong G, Boqian X, Shaoqi C. Performance Analysis of High Speed Floating Ring Hybrid Bearing in the Laminar and Turbulent Regimes[J]. Advanced Materials Research 2011,1167(197-198):1776-1780.

[23] Hong G, Xinmin L, Xiaoling W, et al. Performance of Flat Capillary Compensated Deep/Shallow Pockets Hydrostatic/Hydrodynamic Journal-Thrust Floating Ring Bearing[J]. Tribology Transactions, 2009,52(2):204-212.

[24] Wang X, Li H, Meng G. Rotordynamic coefficients of a controllable magnetorheological fluid lubricated floating ring bearing[J]. Tribology International,2017,1141-14.

[25] Zhongliang X, Weidong Z. An investigation on the lubrication characteristics of floating ring bearing with consideration of multi-coupling factors[J].Mechanical Systems and Signal Processing, 2022,162.

[26] Yi Z ,Wei W ,Daogao W , et al.Coupling analysis of tribological and dynamical behavior for a thermal turbulent fluid lubricated floating ring bearing-rotor system at ultra-high speeds[J].Tribology International,2022,165.

[27] El-Ghoul Z, John S, Dimkovski Z, et al. Wear analysis of pin and roller surfaces[J]. Journal of Physics: Conference Series,2019,1183(1):012007 (13pp).

[28] Alakhramsing S S, Rooij D B M, Schipper J D, et al. A full numerical solution to the coupled cam-roller and roller-pin contact in heavily loaded cam–roller follower mechanisms[J]. Proceedings of the Institution of Mechanical Engineers, Part J: Journal of Engineering Tribology,2018,232(10).

[29] Alakhramsing S S, Rooij D M ,Schipper J D, et al. Lubrication and frictional analysis of cam–roller follower mechanisms[J]. Proceedings of the Institution of Mechanical Engineers, Part J: Journal of Engineering Tribology,2018,232(3):347-363.

[30] Alakhramsing S S, et al. A Mixed-TEHL Analysis of Cam-Roller Contacts Considering Roller Slip: On the Influence of Roller-Pin Contact Friction[J]. Journal of Tribology,2019,141(1):

[31] YUAN J G. Study on high pressure common rail pump floating bearing capability[D]. Shanghai: Shanghai Jiao Tong University, 2010.

[32] LI Z. Research on lubrication characteristics of floating ring bearings of high pressure piston pump[D]. Chongqing: Chongqing University of Technology, 2022.

[33] Xiao Y, Huang D, Guo Y, et al. Parameter Design of Friction Pair of High-Pressure Pump Roller for Marine Engine and Simulation of Double-Layer Oil Film Lubrication[C]//2024 2nd International Conference on Design Science (ICDS). IEEE, 2024: 1-6.

[34] Guo H, Li Y, Zhao B, et al. Transient lubrication of floating bush coupled with dynamics and kinematics of cam-roller in fuel supply mechanism of diesel engine[J]. Physics of Fluids, 2024, 36(12).

[35] LIAO Haiping, LIU Qiyue, ZENG Cuihua, et al. Elastohydrodynamic lubrication design on disc shaped cam mechanism of flat bottomed rectilinear translation follower[J]. Journal of machine design, 2009, 26(5): 71-73.

[36] Matthews J, Sadeghi F, Cipra J R .Radius of Curvature and Entraining Velocity of Cam Follower Mechanisms[J].Tribology Transactions,2008,39(4):899-907.

[37] PATIR N, CHENG H S. Application of average flow model to lubrication between rough sliding surfaces[J]. Journal of Lubrication Technology, 1979, 101(2): 220-229.

[38] Tala-Ighil N, Fillon M. A numerical investigation of both thermal and texturing surface effects on the journal bearings static characteristics[J]. Tribology International,2015,90228-239.

[39] Z.M. Zhang, Fluid Dynamic Lubrication Theory of Sliding Bearings, Higher Education Press (1986).